Raman-induced magnetic resonance imaging of atoms in a magneto-optical trap

T. A. Savard, S. R. Granade, K. M. O'Hara, M. E. Gehm, and J. E. Thomas
Department of Physics, Duke University, Durham, North Carolina 27708-0305
(Received 21 April 1999; revised manuscript received 16 July 1999)

We apply Raman-induced resonance imaging techniques to determine, with a spatial resolution of 12 μm, the size of a cloud of atoms in a magneto-optical trap and the location of the centroid with respect to the magnetic-field zero point. These experiments provide a starting point for developing much higher-resolution resonance imaging methods for cold trapped atoms. [S1050-2947(99)08312-2]

PACS number(s): 32.80.Pj

I. INTRODUCTION

Precision position measurement and localization of atoms in beams and in traps have diverse applications in atom optics. These range from direct-writing neutral atom nanolithography [1] to new fundamental studies of quantum correlations in ultracold, dilute samples of bosons or fermions [2–6]. Further, textbook examples of quantum measurement are enabled by position-dependent atom-field couplings which entangle the atomic internal and center-of-mass states [7,8]. To fully explore these applications, new methods of imaging moving atoms are needed that have the potential to achieve both sub–de Broglie wavelength and suboptical wavelength resolution [2,3].

High-resolution methods based on resonance imaging have been used to determine one-dimensional position distributions in atomic beams [9,10]. In resonance imaging, transitions are induced between two states in the presence of a spatially varying potential which makes the transition resonance frequency dependent on the atomic position. Using an allowed optical transition, this method has been applied to study channeling of atoms in the nodes of a standing wave [9]. Using Raman transitions to obtain a transit-time-limited linewidth in a high-magnetic-field gradient, micron resolution has been achieved in an atomic beam [11]. A suboptical wavelength resolution of 200 nm has been obtained by Raman-induced resonance imaging in the much steeper light-shift gradient of a focused laser beam. In this case, centroids of localized atomic distributions have been determined to within 20 nm [12].

In contrast, the application of high-resolution resonance imaging methods to atom traps has been relatively unexplored. Helmerson *et al.* [13] used laser spectroscopy to measure a one-dimensional distribution of atoms in a superconducting magnet trap. Their resolution was limited by Doppler shifts to approximately 3.5 mm, which is larger than the diameter of many magneto-optical traps (MOT's). Rudy *et al.* [14] used the position-dependent spontaneous scattering rate to investigate the distribution of atoms trapped in a standing wave. Recently, Strekalov *et al.* [15] have developed a method of measuring the velocity and position distributions of cold atomic clouds by observing the temporal shape of photon echoes induced from a coherence grating created between magnetic sublevels.

In this paper, we apply Raman-induced resonance imaging to a cloud of atoms in a MOT in order to determine the size of the position distribution and the location of the centroid. The magnetic-field gradient of the MOT itself provides the necessary position-dependent potential. Atomic positions are determined with respect to the magnetic-field zero point with a resolution of 12 μm. The shapes of the Raman spectra are found to be quite sensitive to the size of the cloud and the direction and magnitude of the offset of the centroid. As described below, improvements can be made to surpass the typical resolution of several microns achieved by CCD-based absorption-fluorescence imaging [16,17].

The Raman imaging technique is applicable to both optically thin and optically thick samples. In the latter case, the high spectral resolution of the Raman method ensures that the fields interact with only a small number of atoms, minimizing distortion arising from absorption. We show how unwanted spatially varying light shifts from the Raman fields can be eliminated and we derive the general structure of the Raman transition probability for alkali-metal atoms in a magnetic-field gradient. This paper serves as a starting point for the development of general resonance imaging methods that will enable the measurement of position distributions and state-dependent spatial correlations of atoms in ultracold vapors with suboptical wavelength, uncertainty-principle-limited precision [3].

This paper is organized as follows. First, we describe the essential features of Raman-induced resonance imaging and derive the transition probability as a function of position in a magnetic-field gradient. We show how this result relates the distribution of atoms in a MOT to Raman-induced resonance imaging data. Then, we present experimental Raman spectra which we use to determine the size and location of the centroid of the spatial distribution of ^{6}Li atoms in a MOT. Finally, we describe potential improvements to increase the resolution of this technique and to use it for tomographic imaging.

II. THEORY

In Raman-induced resonance imaging [2,3], a Raman transition between a populated initial state and an unpopulated final state is driven by two light fields with a relative frequency ω, defined as the Raman difference frequency. Line broadening arising from laser frequency jitter is eliminated by generating the Raman fields from a common laser source using modulation. For copropagating fields, Doppler broadening also is eliminated. Hence, for transitions between

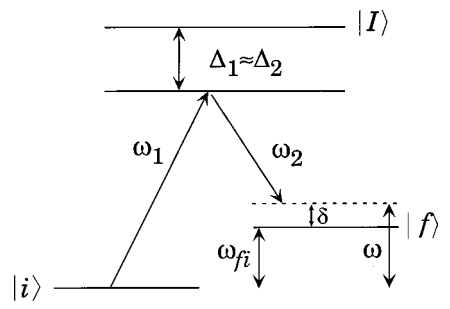

FIG. 1. Energy-level diagram for the Raman transition.

long-lived ground-state sublevels, interaction-time-limited spectral resolution is obtained.

A spatially varying magnetic field shifts the energies of the initial and final states of the Raman transition. For a given difference frequency ω, only atoms which are located at a position with the appropriate magnetic-field strength will make the transition from the initial state to the final state. Hence, by measuring the total number of atoms in the final state as a function of ω, the position distribution for the initial state is determined. The final-state population is determined by probe-induced fluorescence.

The number of atoms N_f transferred by a Raman pulse from the given initial state $|i\rangle$ to the final state $|f\rangle$ is given by

$$N_f(\omega) \simeq \int d^3\mathbf{r} P_f(\omega,\mathbf{r}) n(\mathbf{r}), \tag{1}$$

where ω is the Raman difference frequency, $n(\mathbf{r})$ is the density of atoms in the initial state, and $P_f(\omega,\mathbf{r})$ is the single-atom transition probability which determines the spatial resolution. Strictly speaking, the atoms move during the measurement time, so that the spatial resolution also depends on the momentum of the atoms in the initial state [3]. However, in this experiment our measurements occur on a short enough time scale that the atomic motion is negligible and the momentum dependence of the transition probability can be neglected. In this case, the spatial resolution is determined by the spectral resolution of the short Raman pulse.

In the following, we present the theory for a three-level atom, then modify it as necessary to treat multilevel atoms in a spatially varying magnetic field. By calculating the probability for an atom to make a transition to the final state, we find $P_f(\omega,\mathbf{r})$. Then, using Eq. (1), we characterize the spatial distribution $n(\mathbf{r})$ by fitting a calculated $N_f(\omega)$ to the measured one.

Figure 1 depicts the energy levels and optical frequencies involved in the Raman transition. The atoms are initially in state $|i\rangle$. The Raman pulse contains two optical fields with frequencies ω_1 and ω_2 which couple $|i\rangle$ to $|f\rangle$ through an intermediate excited state $|I\rangle$. As shown, both optical fields are detuned from resonance with $|I\rangle$ by roughly equal frequencies Δ_1 and Δ_2. The resonance frequency for transitions between the states $|i\rangle$ and $|f\rangle$ is $\omega_{fi} \equiv \omega_f - \omega_i$, and the Raman difference frequency is $\omega \equiv \omega_1 - \omega_2$. The Raman detuning is then given by $\delta \equiv \omega - \omega_{fi}$.

If the optical detunings Δ_1 and Δ_2 are large compared to the Rabi frequency and the excited-state radiative decay rate, then the excited-state amplitudes can be adiabatically eliminated, reducing the problem to that of a two-level atom with an effective Rabi frequency given by the Raman Rabi frequency β:

$$\beta = -\sum_I \frac{\langle f|\boldsymbol{\mu}\cdot\mathbf{E}_2^*|I\rangle\langle I|\boldsymbol{\mu}\cdot\mathbf{E}_1|i\rangle}{2h^2\Delta_I}. \tag{2}$$

$\boldsymbol{\mu}$ is the electric dipole operator, $\mathbf{E_1}$ and $\mathbf{E_2}$ are the electric fields of the two Raman beams, and $\Delta_I \approx \Delta_1 \approx \Delta_2$ for each of the intermediate states.

The transition probability for a two-level atom interacting with a square pulse of length τ is well known, and takes the form

$$P_f = \frac{|\beta|^2}{|\beta|^2+\delta^2} \sin^2\left(\frac{\tau}{2}\sqrt{|\beta|^2+\delta^2}\right),$$

where $|\beta|\tau$ is the Raman pulse area. In the experiments, both the detuning and the Rabi frequency are position dependent, as described in the Appendix. The numerical analysis is greatly simplified by using an approximate form for P_f that is given by

$$P_f \simeq \sin^2\frac{|\beta|\tau}{2}\,\mathrm{sinc}^2\frac{\delta\tau}{2}. \tag{3}$$

Here $\mathrm{sinc}\,x = \sin x/x$. When integrated over frequency δ, the approximate form has the same area as the exact result within a few percent for $0 \leqslant |\beta\tau| \leqslant \pi$ and enables analytic evaluation of a radial integral that appears in Eq. (1).

We use this simple two-level-atom result to calculate the Raman transition probability for an alkali-metal atom in a spatially varying magnetic field. In general, the selection rule $\Delta m_F = 0, \pm 1, \pm 2$ governs a Raman transition, since it is a two-photon process in which one photon is absorbed and one is emitted. However, in our experiments, the detunings of the optical beams are large compared to the hyperfine splitting of the excited state, but small compared to the fine-structure splitting. In this case, the nuclear angular momentum acts as a bystander and the J basis determines the structure of the ground-state interaction operator. Since the ground state for an alkali metal has $J = 1/2$, the effective ground-state Hamiltonian can contain only rank-0 and rank-1 operators, and must be a scalar with respect to rotations of the entire system. Hence, for linearly polarized fields, it takes the form

$$H'_{\mathrm{eff}} = |\mathbf{E}_1|^2 T_1^{(0)} + |\mathbf{E}_2|^2 T_2^{(0)} + (\mathbf{E}_1 \times \mathbf{E}_2)\cdot\mathbf{T}^{(1)}. \tag{4}$$

The first two terms describe the light shifts induced by the Raman fields $\mathbf{E}_1$ and $\mathbf{E}_2$. Since these operators are scalar, the light shift for each ground hyperfine state $|F,m_F\rangle$ is independent of m_F. In the experiments, we choose the magnitudes of $\mathbf{E}_1$ and $\mathbf{E}_2$ such that the total light shifts of the $F = 1/2$ and $F = 3/2$ levels are the same. The last term describes the Raman transition operator, which is maximized for $\mathbf{E}_1 \perp \mathbf{E}_2$. Since the Raman transition operator $\mathbf{T}^{(1)}$ is rank 1, only $\Delta m_F = 0, \pm 1$ transitions are allowed. Since no rank-2 transition operator exists for a $J = 1/2$ state, $\Delta m_F = \pm 2$ transitions are forbidden. Equivalently, this result also can be shown to arise by destructive interference between the multiple paths from the initial to the final state.

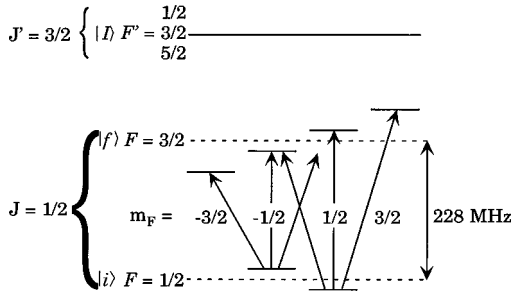

FIG. 2. Possible Raman transitions within the $J=1/2$ ground state of ^{6}Li in the presence of a magnetic field.

In our experiments with ^{6}Li, Raman transitions from $|i\rangle = |F=1/2\rangle$ to $|f\rangle = |F=3/2\rangle$ are induced by two separate, perpendicularly polarized optical beams. As shown in Fig. 2, transitions for different m_F levels are Zeeman split by the applied magnetic field. If the magnetic field splits the m_F levels by more than the linewidth of the Raman transition, then only one transition is resonant for each atom at any particular Raman difference frequency. In this limit, we can treat each Raman transition independently.

The MOT forms near the center of a quadrupole magnetic field, so the magnitude of the field continually increases over the range of the atomic distribution. Thus the multiple two-level approximation is valid for atoms which are far enough from the zero point of the magnetic field. In our experiments, Raman transitions of atoms which are more than 18 μm from the magnetic center are split by more than the Raman linewidth, and can be treated by this approximation. Since the radius of the atomic distribution is approximately 350 μm, the number of atoms which may not be treated by this approximation is a fraction of 1% of the total, assuming that the density distribution varies smoothly (see below). Hence we neglect the contribution made by those atoms to the final-state population in calculating the Raman spectrum.

Since each Raman transition is treated as an independent two-level transition with its own Raman Rabi frequency and detuning, the probability for an atom to be transferred to the final state is simply the sum of the individual transition probabilities given by Eq. (3),

$$P_f(\mathbf{r},\delta)=\frac{1}{2}\sum_i \sin^2\left(\frac{\beta_i(\mathbf{r})\tau}{2}\right)\mathrm{sinc}^2\left(\frac{[\delta-\delta_i^B(\mathbf{r})]\tau}{2}\right), \quad (5)$$

where the sum is over the allowed transitions, and β_i denotes the magnitude of the corresponding Raman Rabi frequency. The factor of $\frac{1}{2}$ occurs because we assume that atoms in the MOT have an equal probability to be initially in either of the $m_F=\pm 1/2$ sublevels of the $F=1/2$ hyperfine state. The shifts $\delta_i^B(\mathbf{r})$ of the Raman transitions in the presence of a weak magnetic field are determined by the Zeeman shifts of the initial and final states, and may be expressed as

$$\delta_i^B(\mathbf{r})=\gamma_{fi}\mu_B B(\mathbf{r})/\hbar, \quad (6)$$

where γ_{fi} is the difference in the products of the Landé g factor and the m_F of the final and initial states, μ_B is the Bohr magneton, and $B(\mathbf{r})$ is the magnitude of the magnetic field. γ_{fi} is zero for the $|F,m_F\rangle = |1/2,1/2\rangle \rightarrow |3/2,-1/2\rangle$ and $|1/2,-1/2\rangle \rightarrow |3/2,1/2\rangle$ transitions. Hence those transitions are independent of magnetic field, and both occur at $\delta=0$. The values of γ_{fi} for transitions in this system are given in Table I.

TABLE I. Values of γ_{fi} for different initial and final states.

			$\|f\rangle$:	$F=3/2$		
		m_F	$-3/2$	$-1/2$	$1/2$	$3/2$
$\|i\rangle$:	$F=1/2$	$1/2$		0	2/3	4/3
		$-1/2$	$-4/3$	$-2/3$	0	

The effect of the magnetic field on the Raman Rabi frequencies $\beta_i(\mathbf{r})$ in Eq. (5) is more complex, and is covered in the Appendix, where the final form of $P_f(\mathbf{r},\delta)$ is given in Eq. (A8). This probability is for one atom at a particular position in the magnetic field. To determine the transition probability for the entire spatial distribution, we multiply $P_f(\mathbf{r},\delta)$ by the atomic density $n(\mathbf{r})$ and integrate over the volume of trapped atoms. Thus the number of atoms that are detected in the final state is

$$N_f(\delta)=\int d^3\mathbf{r} P_f(\mathbf{r},\delta)n(\mathbf{r}). \quad (7)$$

III. EXPERIMENT

The experimental arrangement is shown in Fig. 3. We use a standard $\sigma_\pm$ MOT to confine the atoms. The gradient magnets which are used to form the MOT also create the magnetic potential which is needed for Raman imaging. The local field relative to the magnetic field zero point is given by

$$\mathbf{B}(\mathbf{r})=2B'x\hat{\mathbf{x}}+B'y\hat{\mathbf{y}}+B'z\hat{\mathbf{z}}. \quad (8)$$

Hence the field magnitude is $B(\mathbf{r})=B'\sqrt{(2x)^2+y^2+z^2}$, where $B'=16.5$ G/cm is the field gradient along $\hat{\mathbf{y}}$ and $\hat{\mathbf{z}}$.

The imaging procedure is as follows. After the MOT has formed and the number of atoms has reached equilibrium, the laser beams which form the MOT are momentarily turned off. At this point, atoms are in both the $F=3/2$ and 1/2 hyperfine ground states. An optical pumping beam is used to transfer all of the atoms to the $F=1/2$ hyperfine state. The time scale over which optical pumping occurs, roughly 15 μs, is short enough that significant atomic motion compared to the dimensions of the MOT does not occur.

After the optical pumping beam is turned off, an 8.8-μs Raman pulse with a well-defined difference frequency is applied. Only atoms located in a magnetic field of a particular

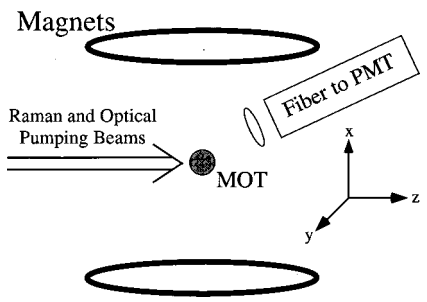

FIG. 3. Scheme of the experiment.

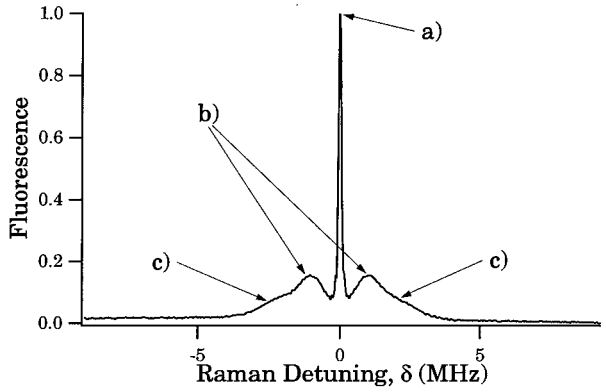

FIG. 4. A typical Raman spectrum, showing the expected five peaks: (a) the magnetic-field-independent resonance; (b) the two narrow magnetic-field-dependent resonances; and (c) the two broad magnetic-field-dependent resonances. The fluorescence intensity is given in dimensionless units, normalized to unity at zero detuning.

strength, which occurs only at a particular set of points in space, are coupled to the final $F=3/2$ state.

The Raman beam intensities are chosen to equalize the light shifts for the $F=1/2$ and 3/2 states. This requires $I_2/I_1=3.1$, where I_1 is the intensity of the beam with higher frequency ω_1 (see Fig. 1). The I_1 beam is $\hat{\mathbf{x}}$ polarized, and the I_2 beam is $\hat{\mathbf{y}}$ polarized. The Raman beams have an elliptical spatial profile, with major and minor widths (full width at half maximum) of 4.8 and 3.6 mm, respectively, large compared to the atom cloud. In our experiments, typical intensities are $I_1=0.07$ mW/mm^2 and $I_2=0.22$ mW/mm^2.

When the Raman pulse ends, the resonant optical pumping beam is turned on again to probe the atoms which have made the transition to the final state. The probe beam causes the $F=3/2$ atoms to fluoresce. The magnitude of the fluorescence is proportional to the total number of atoms in the $F=3/2$ state. Lenses capture this fluorescence and focus it into an optical fiber which leads to a photomultiplier tube (PMT). The voltage generated by the PMT is recorded and the MOT beams are turned back on, reinstating the trapping potential. Additional points in the spectra are obtained by taking measurements at a series of Raman difference frequencies.

A characteristic measured Raman spectrum is shown in Fig. 4. The data in the graph are averaged over 50 spectra taken under identical conditions, then normalized so that the peak height is equal to 1. Of the six possible transitions, two are magnetic field independent, as mentioned in Sec. II, and occur at $\delta=0$. Hence the spectra exhibit five peaks.

The dimensions of the atomic cloud and the location of the centroid relative to the zero point of the magnetic field, are determined from a fit to the Raman spectra. To simplify the analysis, we make some reasonable assumptions about the MOT to reduce the number of parameters which must be fit. We assume that the spatial distribution of atoms in the MOT is described by a Gaussian of the form

$$n(\mathbf{r})=\frac{2}{\pi^{3/2}a^3}\exp(-[4(x-x_0)^2+(y-y_0)^2+(z-z_0)^2]/a^2), \tag{9}$$

where $\mathbf{r_0}=\{x_0,y_0,z_0\}$ is the offset of the MOT centroid from the zero point of the magnetic field, and a is the $1/e$ radius of the atomic distribution along the z and y axes. The axes are defined as shown in Fig. 3. A Gaussian distribution of this form is expected if the MOT acts as an ideal gas that is trapped in a harmonic potential with different restoring forces along the minor and major axes of the MOT ellipsoid [18]. In this case, the ratio of the radii of the MOT ellipsoid along the x and z axes is 1:2, as determined by the inverse of the ratios of the magnetic-field gradients [see Eq. (8)].

In some cases, the spatial distribution of atoms in the MOT may exhibit a two-component structure. For example, a tightly confined component arises from polarization gradient cooling while a larger radius component arises from Doppler cooling [18]. However, for ^{6}Li atoms, where the excited state hyperfine states are nearly degenerate compared to the MOT detunings, polarization gradient cooling for $\sigma_\pm$ molasses is not expected to occur. As described by Dalibard and Cohen-Tannoudji [19], polarization gradient cooling for a standard $\sigma_\pm$ MOT requires rank-2 ground-state operators. Using the same reasoning as described following Eq. (4), rank-2 ground-state operators cannot exist in the ^{6}Li system. Hence we expect that ^{6}Li exhibits only Doppler cooling. This in turn suggests that the spatial distribution is reasonably described by the single-component Gaussian distribution of Eq. (9).

The numerical analysis is greatly simplified by exploiting the symmetry of the magnetic field [Eq. (8)]. We define a coordinate system $x'=2x$, $y'=y$, and $z'=z$. Then we can use a single elliptical radial coordinate r', where $r'^2=4x^2+y^2+z^2$, so that $B(r')=B'r'$ and the surfaces of constant magnetic-field correspond to constant r'. The volume element can be defined as $d^3\mathbf{r}'=dr'r'^2\sin\theta d\theta d\phi$, where θ is the angle between the local magnetic field vector and the Raman beam propagation direction $\hat{\mathbf{z}}$. Equation (A1) then shows that $\sin\theta(\mathbf{r})\rightarrow\sin\theta$, etc., independent of r'.

The location of the centroid, $\mathbf{r}_0'$, can be specified by a shift r_0 and an angle θ_0 relative to the z axis. The azimuthal angle ϕ_0 of the shift cannot be determined due to the spherical symmetry of the magnetic field in the r' coordinate and the cylindrical symmetry of the transition probability about the z axis.

Given these assumptions, we substitute Eqs. (9) and (A8) into Eq. (7), and numerically integrate the result over the new ellipsoidal coordinate system, then fit the resulting spectra to the measured ones. To simplify the integration, we assume that terms in Eq. (A8) with magnetic-field-dependent resonance frequencies are narrow compared to the spectral width of the atomic distribution in the magnetic-field gradient. In this case, the sinc^2 functions can be approximated by δ functions in r'. However, for the central magnetic-field-independent component, we replace the sinc^2 function by a gaussian of unit amplitude which is fit to the measured distribution. This allows us to include line-broadening by a factor of $\simeq 1.3$ due to off-resonant optical pumping. Figure 5 shows that the calculated spectra vary significantly as the physical parameters for the trapped cloud are changed. The reference spectrum is calculated for a trapped atom cloud centered on the magnetic-field zero point, with a z-axis radius of $a=0.5$ mm.

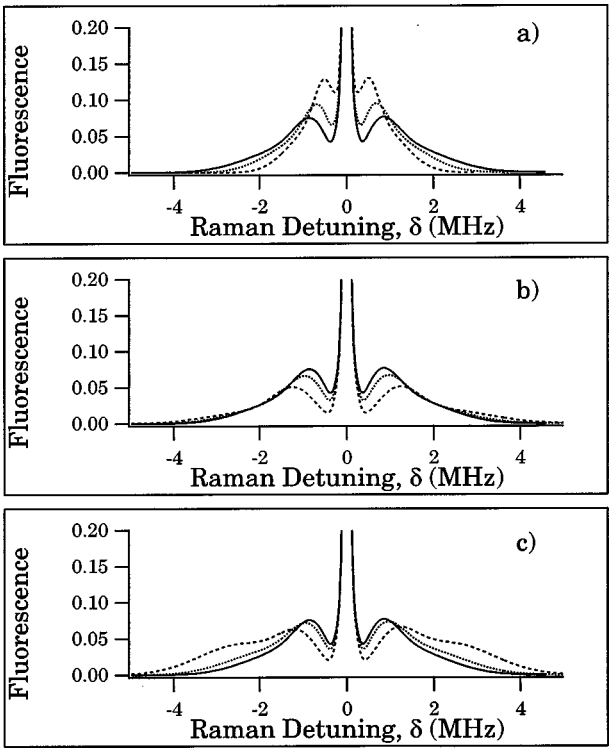

FIG. 5. Calculated spectra for differing spatial distributions: (a) the radius of the atomic cloud is varied, (b) the trap is offset along the x axis, and (c) the trap is offset along the $\hat{\mathbf{z}}$ axis. In (a), the dotted plot is for a 0.4-mm radius, and the dashed plot is for a 0.3-mm radius. In (b) and (c), the dotted plot is for a 0.3-mm offset, and the dashed plot is for a 0.6-mm offset. The reference plot (the solid line in each graph) is calculated for a trapped atom cloud centered on the magnetic field zero with a $1/e$ radius of $a=0.5$ mm along the $\hat{z}$ axis. For each plot, the fluorescence is given in dimensionless units, where the central magnetic-field-independent transition peak is normalized to 1.

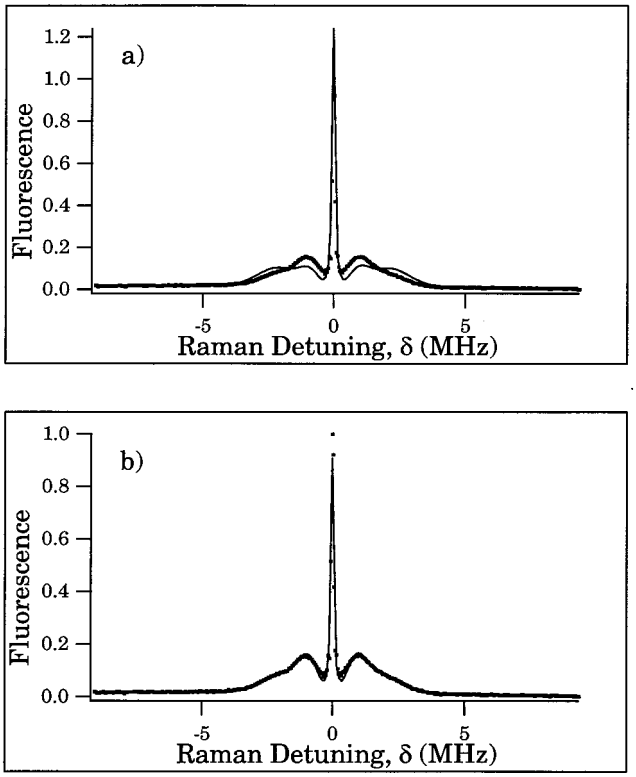

FIG. 6. A comparison of fits when (a) the Raman pulse area is held fixed, and (b) the Raman pulse area is allowed to vary. The dots are data points; the line is the fit to the data. The fluorescence intensity is given in dimensionless units, normalized to unity at zero detuning.

IV. RESULTS

For our data, we made two sets of fits: one in which we allowed the value of the Raman pulse area $\beta_0\tau$ in Eq. (A8) to vary as a fitting parameter, and one in which we held $\beta_0\tau$ fixed. The fits for which we allowed $\beta_0\tau$ to vary were noticeably better at lower MOT laser beam detunings, as shown in Fig. 6. For data taken at the smallest trap detuning, the fitting routine reduced the calculated Raman pulse area to 80% of its estimated value, the minimum allowed by the constraints placed on our fitting routine. For data taken at larger trap detunings, the fitting routine returned a Raman pulse area which was 90% of the estimated value. An error of order 15% in the experimentally estimated Raman pulse area is reasonable.

The $1/e$ trap radius along the z axis is shown in Fig. 7 for different trap laser detunings. The solid line shows the results when the pulse area is held to the estimated value, and the dashed line shows the results when the pulse area is varied by the fitting routine. Both methods indicate the same trends and approximately the same cloud sizes. The error bars denote the square root of the appropriate diagonal element of the covariance matrix determined by the fitting program, and hence the sensitivity of the χ^2 fit to variations in the parameters. The spatial distribution increases in size as the detuning is increased, except at the largest detuning where the size begins to decrease.

Figure 8 shows the trap offset with respect to the magnetic-field zero point. From the fits, we find that the offset is along the $\hat{\mathbf{z}}$ axis. The offset is considerable compared to the size of the trap. Both the fixed and adjustable Raman pulse area fits show the same general trends and magnitudes for the trap offsets. The error bars are computed in the same manner as described in the previous paragraph.

These trap offsets arise from imbalances in the intensity

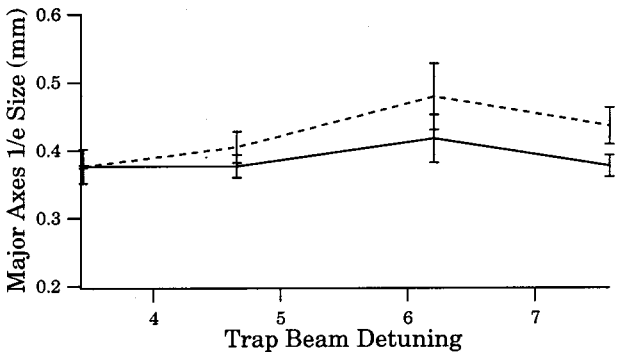

FIG. 7. The $1/e$ trap radius a along the $\hat{\mathbf{z}}$ axis as a function of trap laser beam detuning in units of the natural linewidth ($\gamma=5.9$ MHz). The solid line shows the fit when the pulse area is held constant; the dashed line shows the fit when the pulse area is varied.

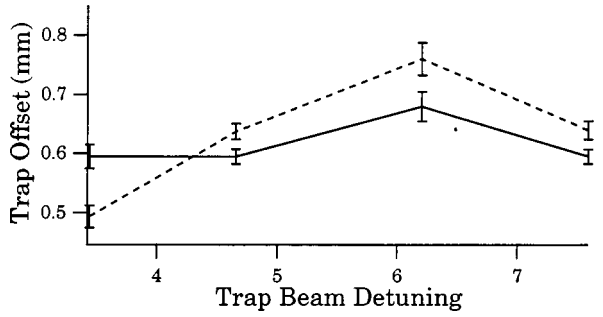

FIG. 8. The offset of the trap along the $\hat{\mathbf{z}}$ axis as a function of trap laser beam detuning in units of the natural linewidth ($\gamma = 5.9$ MHz). The solid line shows the fit when the pulse area is held constant; the dashed line shows the fit when the pulse area is varied. The offset perpendicular to the $\hat{\mathbf{z}}$ axis is found to be negligible. Note that the offset is measured with respect to the magnetic-field zero point.

of the counterpropagating trapping beams. We measured the intensity imbalance to be roughly 10%. Because the center of the distribution will be located where the scattering forces from the forward- and backward-going MOT beams are equal, the center of the MOT shifts from the magnetic-field zero point to a nonzero magnetic-field region where the forces balance. One can show that a 10% intensity imbalance in our experiments easily leads to a trap offset on the order of 1 mm.

V. DISCUSSION

We have applied Raman-induced resonance imaging to determine the size and location of a cloud of atoms in a MOT, relative to the magnetic-field zero point. Since only a small fraction of the atoms is resonant with the Raman pulse at a particular frequency, degrading effects of the trap's optical thickness are reduced compared to resonant optical imaging methods. However, for Raman-induced resonance imaging methods to be generally applicable, it is necessary to develop methods that enable measurement of the position distribution without assuming a particular parametrization. This can be accomplished by using the standard resonance imaging technique of rapidly switching on a bias magnetic field along one spatial axis at a time. Then the magnitude of the total magnetic field is determined primarily by the gradient component parallel to the bias field, while the contributions of the perpendicular components are suppressed. The bias field splits the Raman spectrum so that only one transition is resonant. This enables a one-to-one correspondence between the detected signal and the number of atoms in a given spatial slice perpendicular to the bias field axis, analogous to the methods previously employed in atomic beams [3]. In traps, heterodyne methods can be used to obtained single shot detection as in recent echo experiments [15]. Potentially, very high spatial resolution can be achieved using Raman-induced resonance imaging methods to measure atomic position distributions [3].

In general, the spatial resolution of Raman-induced resonance imaging methods can be limited by the spectral resolution of the Raman pulse $\Delta\nu$, the atomic velocity v_x along the measurement axis, or the atomic acceleration due to the gradient of the magnetic field. Reference [3] gives the following approximate results for spectroscopically limited, velocity-limited, and acceleration-limited position resolutions in a linearly varying potential:

$$\Delta x_{\mathrm{SP}} = \frac{\Delta\nu}{(F_x/h)},$$

$$\Delta x_{\mathrm{VEL}} \simeq \sqrt{\hbar v_x / F_x}, \tag{10}$$

$$\Delta x_{\mathrm{ACC}} \simeq [\hbar^2/(2MF)]^{1/3},$$

where F_x is the differential force exerted by the potential for the inital and final states, and M is the mass of the atom.

In our experiments, the force arises from the spatially-varying Zeeman shift of the levels. For atoms located near the x axis, the magnetic field points nearly in the $\hat{\mathbf{x}}$ direction and transitions occur between the $F = 1/2, m_F = \pm 1/2$ states and the $F = 3/2, m_F = \pm 3/2$ states. The magnetic-field gradient along $\hat{\mathbf{x}}$ is $2B' = 33$ G/cm. From Eq. (6), the differential force is then $F_x/h = \frac{4}{3}\mu_B/h \times 33$ G/cm $= 62$ MHz/cm.

The spectroscopic resolution $\Delta\nu$ is estimated by fitting a Gaussian distribution to the central, magnetic-field-independent component of the measured Raman spectra. We find a half-width at $1/e$ of 77 kHz. This yields a spatial resolution along the x axis of $\Delta x_{SP} = 12.4$ μm. The corresponding resolutions for atoms located near the y and z axes are found to be 25 and 50 μm, respectively. Note that one can obtain equal resolutions along all axes by directing the Raman beams along the symmetry axis of the gradient magnets.

At the typical 1-mK temperatures of our ^{6}Li MOT, the atomic velocity is $\simeq 2$ m/s. Using this and Eq. (10) yields a velocity-limited resolution along the x axis of 7 μm. Velocity x-limited resolution of a few microns can be simply obtained by further cooling the atoms before imaging. Equation (10) shows that, for very cold atoms, the acceleration-limited resolution is 509 nm.

It follows from these estimates that the dominant limitation in our experiments is the spectral resolution. By simply increasing the detuning of the intermediate state of the Raman transition, radiative broadening arising from off-resonant transitions can be reduced. This improves the spectral resolution to the limit determined by the length of the Raman pulse, which can be made long.

Nanometer resolution can be obtained with very steep light shift gradients or magnetic-field gradients. For example, the μ-tip trap described in Ref. [20] has a magnetic gradient of 3×10^5 G/cm. In that trap, Eq. (10) shows that the spatial resolution for a lithium atom near $\mathbf{B} = \mathbf{0}$ would be acceleration-limited to ~ 24 nm.

In conclusion, this paper constitutes a first step in the development of high-resolution resonance imaging methods for cold atoms in traps. Such methods will be important for determining spatial distributions for atoms in optical microtraps, where the length scales of interest can be very small. Resonance imaging methods may be particularly useful in systems where measurement in only one dimension is required. For example, in a tightly confining Gaussian laser beam trap at sufficiently low temperature, all atoms will be in the lowest radial eigenstate. In this case, interesting two-

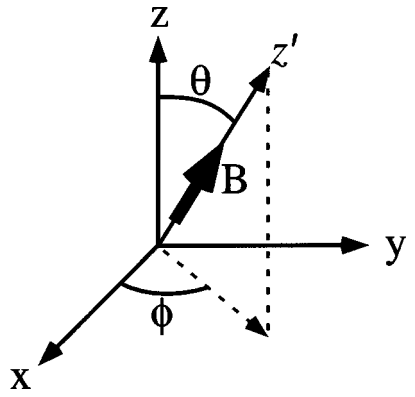

FIG. 9. Orientation of the quantization axis $\hat{\mathbf{z}}'$. The primed axes are the atom frame coordinates, determined by the components of the magnetic field; the unprimed axes are the lab frame coordinates. The $\hat{\mathbf{z}}$ axis is the propagation direction of the Raman fields.

point spatial correlations occur only in the axial direction. Measurement of state-dependent spatial correlations will be of great interest in exploring fundamental quantum features of cold, weakly interacting atom samples [3], such as two-state fermionic atoms in a far detuned optical trap [23].

ACKNOWLEDGMENTS

This work was supported by the U.S. Army Research Office and the National Science Foundation.

APPENDIX: RAMAN TRANSITION PROBABILITY IN A SPATIALLY VARYING MAGNETIC FIELD

The local magnetic field defines a quantization axis, as shown in Fig. 9. In the lab frame, the Raman fields are cross-polarized along $\{\hat{\mathbf{x}},\hat{\mathbf{y}}\}$ and propagate along the $\hat{\mathbf{z}}$ axis. If the local magnetic field $\mathbf{B}$ points along $\hat{\mathbf{z}}$, then the atom experiences the Raman transition operators as defined in the lab. Thus an atom in this magnetic field is coupled to the final state by a $\Delta m=0$ transition. However, if the local magnetic field is oriented along the lab $\hat{\mathbf{x}}$ axis, the atom views the Raman field as being polarized along the $\{\hat{\mathbf{z}}',\hat{\mathbf{x}}'\}$ axes, resulting in $\Delta m=\pm 1$ transitions. In a magnetic field which does not lie directly along one of the lab frame axes, the atoms make a combination of both types of transitions.

The angles θ and ϕ in Fig. 9 depend on the direction of the local field at the point of interest. In the lab frame, the angles are given by

$$\cos\theta(\mathbf{r})=\frac{B_z(\mathbf{r})}{\sqrt{B_x^2(\mathbf{r})+B_y^2(\mathbf{r})+B_z^2(\mathbf{r})}},$$

$$\sin\theta(\mathbf{r})=\frac{\sqrt{B_x^2(\mathbf{r})+B_y^2(\mathbf{r})}}{\sqrt{B_x^2(\mathbf{r})+B_y^2(\mathbf{r})+B_z^2(\mathbf{r})}},$$

$$\cos\phi(\mathbf{r})=\frac{B_x(\mathbf{r})}{\sqrt{B_x^2(\mathbf{r})+B_y^2(\mathbf{r})}},$$

$$\sin\phi(\mathbf{r})=\frac{B_y(\mathbf{r})}{\sqrt{B_x^2(\mathbf{r})+B_y^2(\mathbf{r})}}. \tag{A1}$$

Though the Raman field vectors remain constant in the lab, the quantization axis rotates with the magnetic-field orientation by the angles defined in Eqs. (A1). Thus we can determine the effective Raman Rabi frequencies $\beta_i(\mathbf{r})$ for transitions in the rotated frame $\{\hat{\mathbf{x}}',\hat{\mathbf{y}}',\hat{\mathbf{z}}'\}$ by considering rotations of the Raman transition operator. Since we define the Raman polarizations as $\{\hat{\mathbf{x}},\hat{\mathbf{y}}\}$ in the lab, the unrotated operator T_z induces $\Delta m=0$ transitions. For these transitions, the Raman Rabi frequency is given by [21] $\beta=2\sqrt{2}\beta_0/9$. β_0 is defined as

$$\beta_0=-\frac{\Omega_0^2}{2\Delta}\sqrt{\frac{I_2}{I_1}}. \tag{A2}$$

Δ is the detuning of the Raman beams from the excited state frequency (-118 MHz in our experiment), I_2/I_1 is the ratio of the intensities of the two Raman beams. Ω_0 is an effective Rabi frequency for the strongest transition (the $|F,m_F\rangle=|3/2,3/2\rangle\rightarrow|5/2,5/2\rangle$ transition in our experiment) and is given by

$$\Omega_0=\frac{\mu_0 E_1}{\hbar}, \tag{A3}$$

where E_1 is the electric field of the $\hat{\mathbf{x}}$-polarized Raman beam and μ_0 is the maximum transition dipole matrix element, which is 5.9 D in our experiment.

For brevity, we will only consider transitions from the $|1/2,1/2\rangle$ level of ^{6}Li, since the theory is the same for transitions from the $|1/2,-1/2\rangle$ level. In what follows, $\beta_{i,1/2}$ is the Raman Rabi frequency for $|1/2,1/2\rangle\rightarrow|3/2,i\rangle$ transitions.

Using spherical tensor operator notation $T(k,q)$ [22], we define $T(1,0)=T_z$ where $\langle 3/2,1/2|T_z|1/2,1/2\rangle=\beta_{1/2,1/2}$. In terms of operators in the rotated frame, $T'(1,q)$, $T(1,0)$ may be expressed as [22]

$$T(1,0)=\sum_q T'(1,q)\mathcal{D}^1_{q,0}(\mathbf{r}), \tag{A4}$$

where

$$\mathcal{D}^1_{q,0}(\mathbf{r})=(-1)^q\left(\frac{4\pi}{3}\right)^{1/2}Y_{1,q}(\theta(\mathbf{r}),\phi(\mathbf{r})), \tag{A5}$$

and $Y_{1,q}$ are the spherical harmonics. The angles $\theta(\mathbf{r})$ and $\phi(\mathbf{r})$ are given by Eqs. (A1). Expanding Eq. (A4) using Eq. (A5) gives

$$T(1,0)=T'(1,0)\cos\theta+\frac{1}{\sqrt{2}}T'(1,-1)e^{-i\phi}\sin\theta$$

$$+\frac{1}{\sqrt{2}}T'(1,1)e^{i\phi}\sin\theta. \tag{A6}$$

Since only the magnitude of the Raman Rabi frequency β determines the final-state probability, the phase $\phi(\mathbf{r})$ is not important for determining β. Each of the terms in Eq. (A6) is an operator which couples the initial state $|1/2,1/2\rangle$ to one

of the three final $F=3/2$ states $|3/2,i\rangle$. Here, and in the following, all magnetic quantum numbers are referred to the $\hat{z}'$ axis in the rotated frame. Note that we assume that the populations in the $|1/2,\pm 1/2\rangle$ states are initially equal, so that the initial state has no polarization. Setting $\theta=0$ gives us $\beta_{1/2,1/2}=2\sqrt{2}\beta_0/9$ as the matrix elements of $T(1,0)$ and $T'(1,0)$ for the transition to the $|3/2,1/2\rangle$ state.

The Wigner-Eckart theorem can then be used to determine the remaining matrix elements of the rotated $T'(1,q)$ operator. With the known matrix element of $T'(1,0)$, the reduced matrix element can be determined and is given by $\langle F=3/2||T'(1)||F=1/2\rangle=4\sqrt{3}\beta_0/9$. Using the reduced matrix element, we find that $\langle 3/2,-1/2|T'(1,-1)|1/2,1/2\rangle=2\beta_0/9$ and $\langle 3/2,3/2|T'(1,1)|1/2,1/2\rangle=2\sqrt{3}\beta_0/9$.

Using Eq. (A6) and substituting in the above values of the matrix elements of $T'(1,q)$, the Raman Rabi frequencies in the rotated frame may be written as

$$\beta_{-1/2,1/2}=\frac{1}{\sqrt{2}}\langle 3/2,-1/2|T'(1,-1)|1/2,1/2\rangle\sin\theta=\frac{\sqrt{2}}{9}\beta_0\sin\theta,$$

$$\beta_{1/2,1/2}=\langle 3/2,1/2|T'(1,0)|1/2,1/2\rangle\cos\theta=\frac{2\sqrt{2}}{9}\beta_0\cos\theta,$$

$$\beta_{3/2,1/2}=\frac{1}{\sqrt{2}}\langle 3/2,3/2|T'(1,1)|1/2,1/2\rangle\sin\theta=\frac{\sqrt{6}}{9}\beta_0\sin\theta. \tag{A7}$$

These Raman Rabi frequencies completely specify the contributions to the final state from the $|1/2,1/2\rangle$ state. The contributions from the $|1/2,-1/2\rangle$ state can be calculated in the same manner, giving $\beta_{-3/2,-1/2}=\beta_{3/2,1/2}$, $\beta_{-1/2,-1/2}=\beta_{1/2,1/2}$, and $\beta_{1/2,-1/2}=\beta_{-1/2,1/2}$.

Substituting these values of β_i and the values of $\delta_i^B(\mathbf{r})$ from Eq. (6) into Eq. (5) gives the single-atom final-state probability as a function of position:

$$\begin{aligned}P_f(\mathbf{r},\delta)=&\sin^2\left(\frac{\sqrt{2}}{9}\frac{\beta_0\tau}{2}\sin\theta(\mathbf{r})\right)\mathrm{sinc}^2(\delta\tau/2)\\&+\frac{1}{2}\sin^2\left(\frac{\sqrt{6}}{9}\frac{\beta_0\tau}{2}\sin\theta(\mathbf{r})\right)\\&\times\left\{\mathrm{sinc}^2\left[\frac{[\delta-(4\mu_B/3\hbar)B(\mathbf{r})]\tau}{2}\right]\right.\\&\left.+\mathrm{sinc}^2\left[\frac{[\delta+(4\mu_B/3\hbar)B(\mathbf{r})]\tau}{2}\right]\right\}\\&+\frac{1}{2}\sin^2\left(\frac{2\sqrt{2}}{9}\frac{\beta_0\tau}{2}\cos\theta(\mathbf{r})\right)\\&\times\left\{\mathrm{sinc}^2\left[\frac{[\delta-(2\mu_B/3\hbar)B(\mathbf{r})]\tau}{2}\right]\right.\\&\left.+\mathrm{sinc}^2\left[\frac{[\delta+(2\mu_B/3\hbar)B(\mathbf{r})]\tau}{2}\right]\right\}.\end{aligned} \tag{A8}$$

[1] K. S. Johnson, J. H. Thywissen, N. H. Dekker, K. K. Berggren, A. P. Chu, R. Younkin, and M. Prentiss, Science **280**, 1583 (1998).
[2] J. E. Thomas, Contemp. Phys. **35**, 257 (1994).
[3] J. E. Thomas and L. J. Wang, Phys. Rep. **262**, 311 (1995).
[4] E. V. Goldstein and P. Meystre, Phys. Rev. Lett. **80**, 5036 (1998).
[5] E. V. Goldstein, O. Zobay, and P. Meystre, Phys. Rev. A **58**, 2373 (1998).
[6] K. E. Cahill and R. J. Glauber, Phys. Rev. A **59**, 1538 (1999).
[7] S. Kunze, K. Dieckmann, and G. Rempe, Phys. Rev. Lett. **78**, 2038 (1997).
[8] C. J. Hood, M. S. Chapman, T. W. Lynn, and H. J. Kimble, Phys. Rev. Lett. **80**, 4157 (1998).
[9] C. Salomon, J. Dalibard, A. Aspect, H. Metcalf, and C. Cohen-Tannoudji, Phys. Rev. Lett. **59**, 1659 (1987).
[10] J. E. Thomas, Opt. Lett. **14**, 1186 (1989).
[11] K. D. Stokes, C. Schnurr, J. R. Gardner, M. Marable, G. R. Welch, and J. E. Thomas, Phys. Rev. Lett. **67**, 1997 (1991).
[12] J. R. Gardner, M. L. Marable, G. R. Welch, and J. E. Thomas, Phys. Rev. Lett. **70**, 3404 (1993).
[13] K. Helmerson, A. Martin, and D. E. Pritchard, J. Opt. Soc. Am. B **9**, 483 (1992).
[14] P. Rudy, R. Ejnisman, and N. P. Bigelow, Phys. Rev. Lett. **78**, 4906 (1997).
[15] D. V. Strekalov, A. V. Turlapov, A. Kumarakrishnan, S. B. Cahn, and T. Sleator, Bull. Am. Phys. Soc. **44**, 1154 (1999).
[16] D. W. Sesko, T. G. Walker, and C. E. Wieman, J. Opt. Soc. Am. B **8**, 946 (1991).
[17] B. P. Anderson and M. A. Kasevich, Phys. Rev. A **59**, R938 (1999).
[18] C. G. Townsend, N. H. Edwards, C. J. Cooper, K. P. Zetie, C. J. Foot, A. M. Steane, P. Szriftgiser, H. Perrin, and J. Dalibard, Phys. Rev. A **52**, 1423 (1995).
[19] J. Dalibard and C. Cohen-Tannoudji, J. Opt. Soc. Am. B **6**, 2023 (1989).
[20] V. Vuletic, T. Fischer, M. Praeger, T. W. Hänsch, and C. Zimmerman, Phys. Rev. Lett. **80**, 1634 (1998).
[21] T.A. Savard, Ph.D. thesis, Duke University, 1998.
[22] A. R. Edmonds, *Angular Momentum in Quantum Mechanics* (Princeton University Press, Princeton, 1974).
[23] K. M. O'Hara, S. R. Granade, M. E. Gehm, T. A. Savard, S. Bali, C. Freed, and J. E. Thomas, Phys. Rev. Lett. **82**, 4204 (1999).